



Science Arts & Métiers (SAM)

is an open access repository that collects the work of Arts et Métiers Institute of Technology researchers and makes it freely available over the web where possible.

This is an author-deposited version published in: <https://sam.ensam.eu>
Handle ID: <http://hdl.handle.net/10985/23311>

To cite this version :

Rafael PENAS, Arnaud GAUDIN, Etienne BALMES - Hyper-reduced models of hyperelastic dissipative elastomer bushings - In: ISMA2020, Belgique, 2020-09-07 - Proceedings of ISMA 2020 and USD 2020 - 2020

Any correspondence concerning this service should be sent to the repository

Administrator : scienceouverte@ensam.eu



Hyper-reduced models of hyperelastic dissipative elastomer bushings

R. Penas^{1,2}, A. Gaudin¹, E. Balmes^{2,3}

¹ Groupe PSA, Scientific Department and Disruptive Technologies,
France

² HESAM University, PIMM, Arts et Metiers Institute of Technology, CNRS, Cnam,
France

³ SDTools,
France

Abstract

Rubber mount modeling is crucial for correct multibody simulation, but the cost of 3D large deformation finite element computation is orders of magnitude higher than needed for reasonable multibody computation times. As a result, mount characterization is purely experimental and does not allow design studies on shape, material properties or complex loading, that would be a much needed improvement over current practice. The paper first discusses material laws suited for rubber behavior in large deformations, then kinematic reduction combined with fast evaluation of generalized loads using hyper-reduction is introduced as a methodology to obtain acceptable computation times. An industrially representative model is then used to demonstrate the validity of the procedure and gain insight on how it can be used in practice.

1 Introduction

Rubber mounts are widely used in automotive industry due to their capacity to undergo large deformations with low deterioration, to their relatively low stiffness and high dissipative properties. These features make the material appropriate to connect vibrating parts to the chassis, such as powertrain and suspension. Articulation models are mostly used in large multibody systems, where several bodies are connected by different kinds of joints.

Even if joints are not the main object of study for a multibody system, inaccurate models may lead to incorrect system behavior [1]. For practical use, joints must not be a time consuming component, so they are usually modeled with a single integration point model with separate dissipation and conservative parts. While these models may reproduce test campaigns with a fair precision and high performance, there is no possibility of effective identification, shown as the top blue arrow of figure 1, without extensive testing. Testing all the possible load cases in a joint to compile a fully representative model is thus a very expensive process.

The alternative strategy is to consider identification of material properties shown as red arrow in figure 1. Section 2 will however illustrate that elastomer behavior and modeling is still a very open problem. Beyond the complexity of material laws, a passive control of stiffness and dissipation over the operating range often demands the articulations to have complex geometries. An accurate description of these phenomena requires a nonlinear finite element with a high degree of detail on the geometry and therefore a great number of degrees of freedom, leading to simulation times in hours, when seconds are necessary for practical multibody simulation. Thus currently the only possibility to exploit material behavior is to identify meta-models based on numerical experiments similar to those of test campaigns.

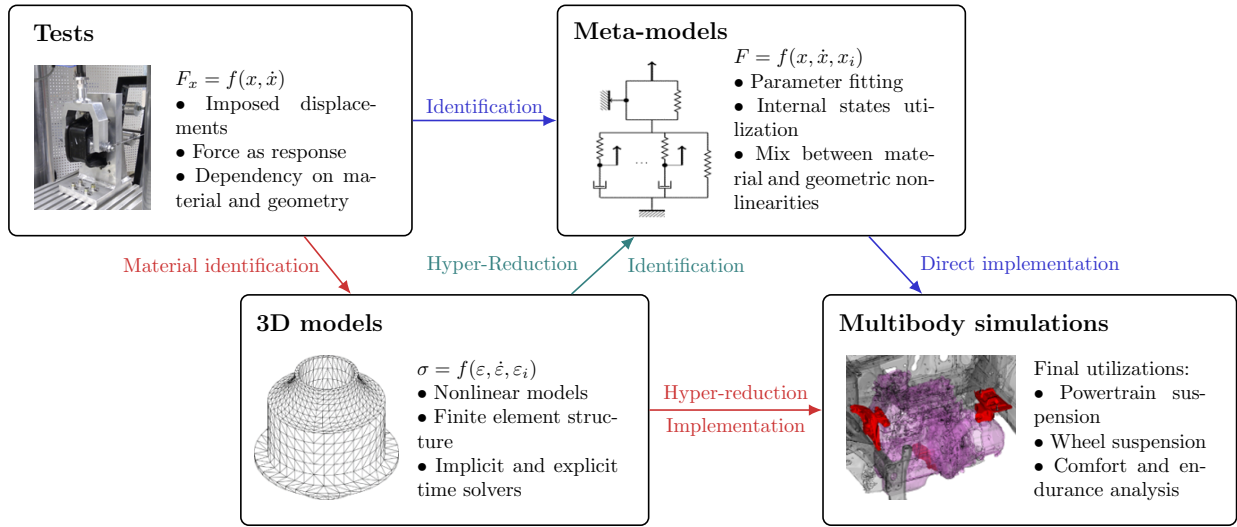


Figure 1: Current (blue) and proposed (green and/or red) procedures for emulating elastic articulations in MBS.

This work thus aims to apply a hyper-reduction technique to a non linear highly detailed model finite element model, and analyze its viability for use in multibody simulations, either directly for the system simulation (bottom red arrow in figure 1) or indirectly to speedup numerical experiments to be used in meta-model identification (green arrow). Issues are thus strategy to achieve a compromise between performance and accuracy by the use of a low order model and analysis of the ability to reuse reduced models in extrapolated conditions not considered in the model building phase. Section 3.1 describes the implementation, in the MATLAB-based Structural Dynamics Toolbox [2], of large transform non-linear material computations, used in the learning phase of the model reduction technique. Section 4 then analyzes the implementation and assesses performance of the method for a realistic test case.

2 Material modeling

Material modeling corresponds to the definition of a constitutive law that determines stresses as a function of a deformation state and its history or internal states. Models that fully capture rubber behavior have been extensively studied [3, 4, 5, 6, 7]. But this work will focus on the ability to use such models in practical MBS applications and thus retain a *somewhat simple* model capturing the base requirements, large deformations, hyperelasticity and viscoelasticity.

2.1 Hyper-elasticity

Given a volume Ω , each material point in the volume may be defined by its resting position noted by a vector x_0 . The current position of this point is noted by x , hence its current displacement may be defined by $u = x - x_0$. From the displacement, it is possible to define the deformation gradient tensor as $F = \mathbb{1} + \nabla u$.

Quadratic forms of the deformation tensors such as the right Cauchy-Green deformation tensor $C = F^T F$, or the left Cauchy-Green deformation tensor $B = F F^T$ are independent from any rotations on the material point and are either related to the base configuration (lagrangean quantities) or to the current configuration (eulerian quantities). Each consistent deformation measure has its energy conjugate stress, and in this work the ones to be used are the pair first Piola-Kirchhoff stress P , and deformation gradient F , which are native to SDT. For the development of a the material behavior, the pair second Piola Kirchhoff stress S with the right Cauchy-Green deformation tensor C will also be used. These stresses are related by the expression $P = F S$.

When leaving the small strain domain, linear elasticity is not suited for most materials [8]. To achieve a reasonable description of conservative forces generated by the material, the most common method is to use an energy functional of strain tensors. Different potentials are analyzed by [9] and here, for simplicity, one chooses a Mooney-Rivlin formulation given by

$$\psi = c_1 I_1 + c_2 I_2 + \frac{\kappa}{2} (I_3^2 + \ln(I_3)), \quad (1)$$

where

$$I_1 = \det F^{-2/3} \text{trace}(C), \quad I_2 = \frac{\det F^{-2/3}}{2} (\text{trace}^2(C) - \text{trace}(C^2)), \quad I_3 = \det(F) \quad (2)$$

are the reduced invariants of the right Cauchy-Green strain tensors, which are deviatoric quantities. Thus, a complete decoupling between deviatoric and compression behaviors is observed on this hyper-elastic model. This separation will be verified for the rest of the model components, and it avoids numerical issues linked to the different magnitudes of forces of these two different natures. Deriving the functional with respect to deformation, stress is obtained

$$S^{HE} = 2 \frac{\partial \psi}{\partial C} = (c_1) \mathbb{1} + c_2 \frac{1}{2} (I_1 \mathbb{1} - C) + \kappa \left(I_3 + \frac{1}{I_3} \right). \quad (3)$$

Numerical stability for this type of model may be assured by the polyconvexity of the potential function ψ [10], which is the case for the chosen model only up to moderate deformations.

2.2 Viscoelasticity in large strains

Figure 2: Rheologic scheme for Maxwell cell model.

Viscoelasticity expresses a behavior dependency on deformation rate, and consequently on loading frequency. For an uniaxial Maxwell material with a number N of viscoelastic cells, as figure 2 shows, the behavior follows the equation

$$\begin{cases} \sigma = E^\infty \varepsilon + \sum_i^N \sigma^i \\ \dot{\sigma}^i + \frac{E^i}{c^i} \sigma^i = E^i \dot{\varepsilon} \end{cases} \quad (4)$$

where E^i are elastic moduli, and c^i are viscous coefficient for each branch, ε^i the uniaxial deformations and σ^i the uniaxial stress for each branch. For this case, response is usually seen in form of complex modulus in frequency domain, as a transfer function

$$E(\omega) = E^\infty + \sum_i^N E^i \left(\frac{\omega^2 \tau^{i2}}{1 + \omega^2 \tau^{i2}} + i \frac{\omega \tau^i}{1 + \omega^2 \tau^{i2}} \right) \quad (5)$$

where τ^i are the time constants c^i/E^i . Tuning for this function can be done by pole-zero allocation [11]. Although, present implementation requires stress time response, which may be written in form of a Prony series,

$$\sigma(t) = E^\infty \left(\varepsilon + \sum_i^N \int_{-\infty}^0 \alpha^i(t-s) \dot{\varepsilon} ds \right), \text{ with } \alpha^i(t) = \frac{E^i}{E^0} (1 - e^{t/\tau^i}). \quad (6)$$

This formulation may be expanded to a 3D model by the use of an energy potential instead of a modulus as the base of relaxation, based on [12], and instead of using an elastic modulus, stresses are to be used directly,

to avoid the necessity to compute a tangent stiffness matrix,

$$\begin{cases} S = \frac{\partial \psi}{\partial C} + H^i \\ \dot{H}^i + \frac{1}{\tau^i} H^i = \frac{g^i}{\tau^i} \frac{\partial \psi}{\partial C} \end{cases} \quad (7)$$

where H^i are viscous stresses in second Piola Kirchhoff form and g^i are relaxation fractions of the full potential ψ . As for the unidimensional case, the solution of the differential equation can be written in terms of Prony series

$$S(t) = g^0 \frac{\partial \psi}{\partial C} + \int_{-\infty}^t \alpha^i(t-x) \frac{\partial \psi}{\partial C}(x) dx, \text{ with } \alpha^i(t) = g^i (1 - e^{-t/\tau^i}) \quad (8)$$

2.3 Implementation

The implementation of the constitutive law is always the part taking most development time, while being critical for performance. The strategy retained here is to optimize a MATLAB implementation and then use automated C++ translation for the actual use. The SDT explicit solver provides deformation gradient, its derivative and internal states. Invariants and deviatoric hyperelastic stress for each cell are computed from equations (2) and (3). To solve the differential equations associated with viscous stress, convolution (8) is not practical in terms of memory so that an explicit integration scheme leading to a recursion equation using internal states is introduced

$$H_n^i = e^{-dt/\tau^1} H_{n-1}^i + e^{-dt/2\tau^1} (S_n^{HE} - S_{n-1}^{HE}), \quad (9)$$

For compressive forces, instantaneous pressure is computed by

$$p = \frac{\kappa}{2} \left(I_{3n} - \frac{1}{I_{3n}} \right). \quad (10)$$

Elastomer materials are very incompressible, and such type of model may generate high frequency oscillation waves, that may destabilize the numerical scheme [13]. For this reason, bulk viscosity was introduced as a mean to dissipate these waves. It relies also on an explicit scheme and leads to the recursion equation

$$p_v = e^{-dt/\tau^p} (I_{3n} - I_{3n-1}). \quad (11)$$

Figure 3 summarizes the various steps of constitutive law implementation.

3 Structural models

A material model by its own is not capable of representing a few important aspects of elastic articulations, such as the stress concentration on certain regions or the stiffening by geometry. To represent these effects accurately, the articulation must be considered as a complex deformable structure apart with multiple degrees of freedom, described by the appropriate material behavior.

3.1 Finite element formulation

The Finite Element method is a well established structural analysis tool. Classically the volume Ω is divided in simple geometric volumes, and any continuous quantity on these elements is interpolated by piecewise polynomial shape functions. Considering kinematic description, the shape functions N_i describe displace-

Material function

$$[F]_n, [\dot{F}]_n, [H^i]_{n-1}, I_{3n-1}, [S^{HE}]_{n-1}$$

$$[C_n] = [F]_n^T [F]_n, [d]_n = \frac{1}{2} [F]_n^{-T} [\dot{C}]_n [F]_n, I_{3n} = \det([F]_n)$$

$$I_{1n} = I_{3n}^{-2/3} \text{trace}([C]_n), I_{2n} = \frac{I_{3n}^{-2/3}}{2} (\text{trace}^2([C]_n) + \text{trace}([C]_n^2))$$

$$[S^{HE}]_n = \text{dev}((c_1) [\mathbb{1}] + c_2 (I_{1n} [\mathbb{1}] - [C]_n))$$

Loop over cells i

$$[H]_n^i = \text{dev} \left(e^{-dt/\tau^i} [H]_{n-1}^i + e^{-dt/2\tau^i} ([S^{HE}]_n - [S^{HE}]_{n-1}) \right)$$

Compressive deformations

$$p_n = \frac{\kappa}{2} \left(I_{3n} - \frac{1}{I_{3n}} \right)$$

$$p_n^v = e^{-dt/\tau^p} (I_{3n} - I_{3n-1})$$

Output

$$[P]_n = [F]_n \left(I_{3n} (p_n + p_n^v) [\mathbb{1}] + \sum_{i=1}^N g^i [H]^i \right)$$

$$\mathcal{U}_{int} = \left\{ \begin{array}{c} I_{3n} \\ [S^{HE}]_n \\ [H]_n^i \end{array} \right\}$$

Get deformation and internal states

Main deformation tensors

Invariants

Deviatoric hyperelastic stress

Loop on viscous cells

Viscous stress

Pressure

Bulk viscosity

Output stress

Internal state propagation

Figure 3: Pseudo algorithm for constitutive law integration.

ment, one can write for the body

$$\{u(x, t)\} = \sum_{i \in \Omega} [N_i] \{q(t)\}, \text{ and } [F(x, t)] = \sum_{i \in \Omega} [N_{i,x,y,z}] \{q(t)\}, \quad (12)$$

where $N_{x,y,z}$ represent the derivative of shape functions that depend on space, q the Degrees Of Freedom (DOF) which depend on time. To standardize the expressions (12) with the input/output formalism used in SDT, it is chosen here to say that displacement gradient can be observed at any point g using a linear function of DOF associated with the observation matrix \mathbb{C} , so that

$$\{F(x_g, t)\} = [\mathbb{C}(x_g)] \{q(t)\} \quad (13)$$

The continuously distributed quantities dual to the displacement gradient are called stresses in mechanics and are obtained from the constitutive modeling discussed in section 2. The principle of virtual work, that ensures energy conservation, is written

$$\int_{\Omega} \rho \ddot{u} dV + \int_{\Omega} P : dF = \int_{\Omega} f du \quad (14)$$

The first integral on the left hand side corresponds to the work of inertia forces, , with ρ the density function for the material, and may be computed by a volume integral approximated by a rule at node to obtain a diagonal mass matrix for explicit time integration. The right hand side term correspond to work made by external forces, which are known a priori here. The remaining term corresponds to work of internal forces, and depends on stress integration over the elements, which may be done by a Gauss quadrature, that may as well be seen as a result of an observation on stresses weighted by the jacobian J of transformation and the quadrature weights w_g ,

$$\mathcal{F}_{int} = \int_{\Omega} P : dV \approx \sum_g \mathbb{C}^T J_g w_g P_g = [\mathbb{B}] \{P_g\}, \quad (15)$$

where \mathbb{B} corresponds to the command matrix associated with stresses. Reciprocity is ensured by the fact that its columns are related to the observation matrix rows by weights $J_g w_g$ at each Gauss point.

The differential equation in time may solved by any integration scheme. Figure 4 shows the explicit Newmark scheme used here [14].

<u>Start step</u>	
$t_n = t_{n-1} + dt, \quad n = n + 1$	Time step and increment
$q_n = q_{n-1} + dt \dot{q}_{n-1/2}$	Compute displacements
$r = -\mathcal{F}_{ext}$	Initialize residual
<u>Compute residual for each Gauss point g</u>	// Loop for each Gauss points
$F_n^g = \mathbb{C} q_n, \quad \dot{F}_n^g = \mathbb{C} \dot{q}_n$	Compute strains and get internal states
$[P_n^g, \mathcal{U}_n^g] = f_{material} \left(F_n^g, \dot{F}_n^g, \mathcal{U}_{n-1}^g \right)$	Compute stresses and evolve internal states
$r = r + \mathbb{B} P_n^g$	Compute residuals on DOF
<u>DOF evolution</u>	
$\ddot{q}_n = -M^{-1} r$	Compute accelerations
$\dot{q}_n = \dot{q}_{n-1} + \frac{dt}{2} \ddot{q}_n + \frac{dt}{2} \ddot{q}_{n-1}$	Compute velocities
$\dot{q}_{n+1/2} = \dot{q}_n + \frac{dt}{2} \ddot{q}_n$	Estimate speed
<u>Store strategy</u>	Store output and
If $\text{mod}(n, Store) = 0$	Subsampling condition
$q_{out} = [q_{out}, q_n], P_{out} = [P_{out}, P_n]$	Store sampled steps
$\mathcal{U}_n \leftarrow \mathcal{U}_{n-1}$	Overwrite internal states

Figure 4: Explicit Newmark scheme

3.2 Kinematic reduction

Kinematic reduction, or classical Ritz analysis, consists on restraining the displacements into a subspace of a considerably smaller rank. This is called model reduction in the modal analysis community, but the term **kinematic** reduction is preferred here since hyper reduction will be introduced as a second ingredient for the reduced models eventually used. In a control community, one would say state reduction. One thus assumes to have a process to build a base T that spans a subspace containing a close approximation of the true solution. In other words

$$\{q(t)\} = [T] \{q_R(t)\}, \quad (16)$$

where q_R are the reduced degrees of freedom. This matrix must have as many lines as the displacement vector q , but the number of columns is an open choice, which will depend on how the base is built. Early methods from the vibration community build bases by combining modes and static correction terms [15], which are related to the singular value decomposition [16] where reduced model building is formulated as a subspace classification problem. Subspace classification has been considered in many applications and fields [17, 18, 19] with keywords such as Singular Value Decomposition, KLD (Karhunen-Loève Decomposition), PCA (Principal Component Analysis), PGD (Proper Generalized Decomposition).

Since, large strain and non-linear material behavior is considered, modes are not directly pertinent and a snapshot building strategy, discussed for example in POD algorithms [17], is considered here. A set of vectors is generated by a high cost (also called off-line) full 3D computation. Snapshots at a regularly spaced timesteps form a matrix q_{learn} . A singular value decomposition of this matrix (possibly weighted with the mass and stiffness matrices [16]) leads to

$$[q_{learn}] = \sum_i \{U_i\} (\sigma_i [v_i(t)]) \quad (17)$$

with U_i the orthonormal left singular vectors giving shapes in space, σ_i the singular values and v_i the right singular vectors giving amplitude dependence as function of time. The reduction is obtained by taking a few of the left singular vectors to form the columns of basis matrix T . The accuracy of the subspace representation is given by the amplitude of the first truncated singular value.

To preserve energy, kinematic reduction is also applied to the test functions used for the virtual work principle. In other words, the observation (13) and command (15) equations, keep the same form with $[\mathbb{C}_R] = [\mathbb{C}] [T]$ and $[\mathbb{B}_R] = [T]^T [\mathbb{B}]$. As the result the implementation of time integration schemes is unchanged. Although there is notable decrease of physical memory requirements, the most time consuming steps related to material law computation remain and kinematic reduction is thus not relevant when a high number of Gauss points is used.

3.3 Hyper-reduction : approximate power integrals

Hyper reduction is a technique that allows, while keeping controlled accuracy, the evaluation of the material law at a small subset of the full model Gauss point set. Recently several different techniques were developed are discussed in [20]. The one used in present work was developed by [21] is known as Energy Conserving Sampling and Weighting (ECSW). The principle is, after a learning phase and kinematic reduction, to perform a reduced integration over the volume, while keeping the same forces generated by each reduced degrees of freedom. The internal forces at all learning time steps can be computed by

$$[\mathcal{F}_{int}^l]_{NR \times NT} = \sum_{g=1}^{NG} [\mathbb{C}T]^T J_g w_g [P_g(t)]_{9 \times NT} \quad (18)$$

where internal forces clearly appear to be a linear combination of weights w_g , so that one can rewrite the equation as

$$\mathcal{F}_{int}^l = [G(P_g(t))] \{w_g\} = [\mathbb{C}T]^T J_g P_g(t)_{(NR \times NT) \times NG} \{w_g\}_{NG \times 1} \quad (19)$$

The matrix G of unassembled forces has a length of the number of the retained vectors for the base times the number of snapshots for the learning phase. The hyper-reduction consists in computing this force contribution for the whole kinematic reduction base and for all learning phase snapshots, and finding a different vector of weights w_g^* which is sparse and keeps the contributions well represented. In other words,

$$\text{Find } w_g^* \text{ that minimizes } \|w_g^*\|_0, \text{ subject to } \left\| [\mathcal{F}_{int}^l] - [G] \{w_g^*\} \right\|_2 < \varepsilon_{tol} \text{ and } w_g^* > 0. \quad (20)$$

Since the optimized result is sparse, one can say that it is a set E of N_g^* hyper Gauss points and associated weights w_g^* leading to an unchanged form of (15) where the set of Gauss points is much smaller and the weights are redefined and incorporate the jacobian

$$\mathcal{F}_{int}(t) \approx \sum_{g^* \in E} [\mathbb{C}T^T w_g^*] \{P_{g^*}(t)\} = [\mathbb{B}_R^E] \{P_{g^*}(t)\}. \quad (21)$$

Although, a minimization with a zero-norm is a problem with NP complexity, a sub-optimal approach, called Sparse Non Negative Least Square method (SNNLSQ), consists in finding the point that contributes the most to respect the constraints, and then perform a regular LSQ with this point and all previously added, until the constraints are satisfied. A summary of the implementation is shown in figure 5.

In the end, the only update made to the model is to make the observation matrix based only on the subset of hyper Gauss points $\mathbb{C}(E)$, while command must have its weights updated.

4 Sample application

While the kinematic reduction/hyper-reduction methodology is now well established, it is not widely implemented and significant efforts should be placed into devising strategies to optimize its use in various applications. The objective of this section is thus to illustrate how the accuracy of the reduced model can be controlled and how its domain of validity can be evaluated.

Learning simulation
 $\mathbb{B}, \mathbb{C}, w_g, P_g^l, T, G$
 $\{\mathcal{F}_{int}^l\} = [G] \{w_g\}$

 Initialize $E = \emptyset, w_g^* = \{0\}$

 Initialize $\varepsilon_{tol}, r = 1$
SNNLSQ
 While $r = \left\| \frac{\mathcal{F}_{int}^l - G \{w_g^*\}}{\mathcal{F}_{int}^l} \right\| > \varepsilon_{tol}$
 $r_0 = \mathcal{F}_{int}^l - [G] \{w_g^*\}$
 $\mu = [G]^T r_0$

 Find index j_μ of $\max(\mu)$
 $E = E \cup j_\mu$
 $\eta = \min_{w_g^*} \left(\|\mathcal{F}_{int}^l - [G] w_g^*\|_2 \right)$

 Find index j_{neg} of $\eta < 0$
 $E = E \setminus j_{neg}$
 $w_g^*(\bar{E}) = 0$ and $w_g^*(E) = \eta$
 $\mathbb{B}_R^E = T^T \mathbb{B}(E) w_g^*, \mathbb{C}_R^E = \mathbb{C}(E) T$

Assembly, learning, kinematic reduction

Get internal forces for training conditions

Initialize set of active points and weights

Initialize hyper-reduced command and tolerance

Optimization loop

Get difference from full internal load learning points

Compute points contributions for current residue

Get point with most contribution

Add Gauss point to active points set

Least square method to find optimal weights

Find computed negative weights

Remove negative weights from active set

Assign weights to active elements

Update observation and command

Figure 5: Implemented hyper reduction scheme

4.1 Full model results

The full model is based on a rear suspension twist beam axle articulation shown in figure 6. It has 77mm of outer diameter and 45.5mm of inner diameter. It is composed by two different elastomer materials surrounded by metal plates. Metal parts are considered rigid and the elastomer volume is modeled by the constitutive law presented in section 2 and constants given in table 1. To reduce the learning phase computational cost, the model is cut in four using its symmetry planes. The retained model uses 24530 hexahedron elements with eight integration points each and a total of 76084 DOF. The exterior shell is fixed and a force is applied to the inner shell as shown in figure 6.

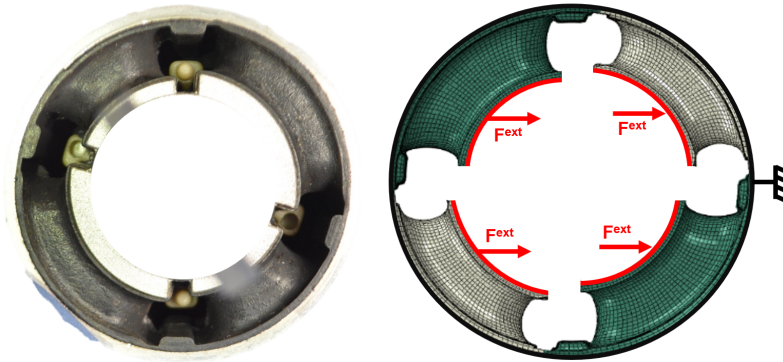


Figure 6: Elastic articulation and finite element model used.

For explicit schemes, the maximum time step is determined from material behavior using [22]

$$\mathrm{d}t_{\max} = L_{\min} \sqrt{\frac{\rho}{\hat{\mu} + \hat{\lambda}}}, \quad (22)$$

where L_{\min} is the length of the smallest element, ρ the material mass density, $\hat{\mu}$ and $\hat{\lambda}$ are the linearized Lamé parameters for the material. Since viscous effects only soften the material model described in section 2, it is safe to assume that the coefficients for the hyperelastic stress would enable the computation of the maximum stable time-step.

Table 1: Material constants used in simulation.

c_1	c_2	κ	κ_v	g	τ	ρ
1MPa	2MPa	20MPa	0.2MPa	$1/3, 1/3$	$1/12s, 1/50s$	2.33 ton/m ³

The learning phase consists in the simulation of 3 cycles at 20Hz. The computation took 27.7 hours in a Core i5-6300HQ CPU at 2.3GHz. Timestep used is 30% superior to the one computed by (22). The constitutive law was called 49.06×10^9 , times, for 250×10^3 timesteps. The most deformed element peaks at 37% deformation. Snapshot sampling is made to get 30 sample points per cycle for the hyper-reduction step.

4.2 Performance Assessment

The SVD from the learning phase results takes only a few seconds as less than a hundred snapshots are used. For kinematic reduction, 6 shapes are retained, defined by a threshold of 1% from the most significant singular value. First five shapes are shown in figure 7 along with the decrease of singular values. The least important singular shapes show already localized deformations, which means that retained shapes should be enough to capture global deformations in the model.

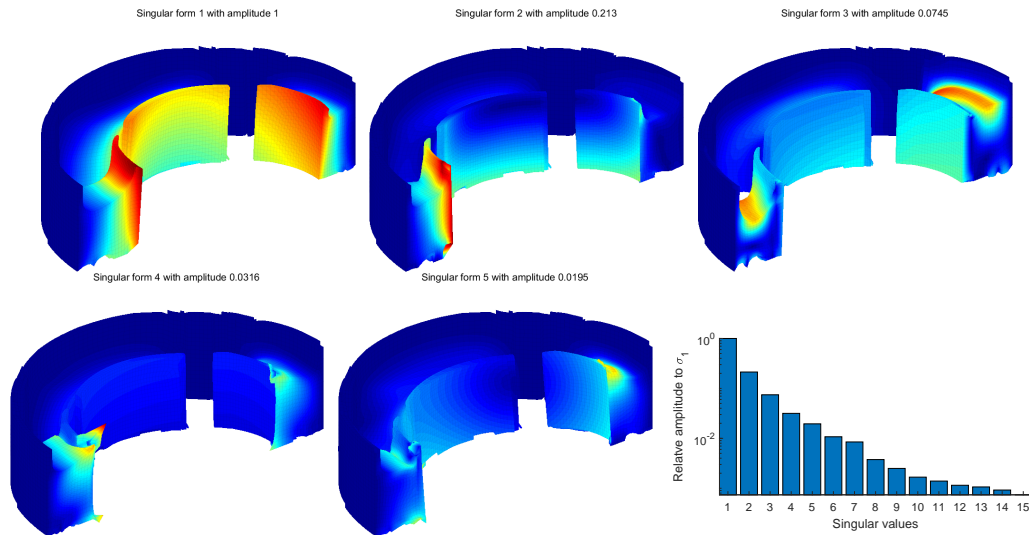


Figure 7: First 5 vectors from the reduced model base and singular values amplitudes

For the hyper-reduction, a few minutes are needed to converge with the chosen kinematic base and a tolerance of 10^{-4} on full internal work contributions. The final model retains 139 Gauss points out of 196240, meaning a 3 orders of magnitude reduction, which can be directly translated to CPU time as illustrated in table 2.

Table 2: Model characteristics. CPU time is for 3 cycle transient.

	Number of DOF	Number of Gauss points	CPU time
Full model	76084	196240	27.7h
Hyper reduced with 3 cycles	6 (10^{-2} on tolerance)	139 (10^{-4} on tolerance)	29s
Hyper reduced with half cycle	4 (10^{-2} on tolerance)	48 (10^{-4} on tolerance)	12s

Figure 8 illustrates the distribution of those hyper Gauss points. The distribution of the points is mainly concentrated on traction/compression zones, indicating, as expected, that these regions are those where the material behavior is more non-linear.

Simulation on the hyper-reduced model takes less than 30 seconds on the same CPU, corresponding to a speedup factor above 2000 (as shown in table 2). Figure 9 shows the very good match of the global displacement of the full and hyper-reduced models.

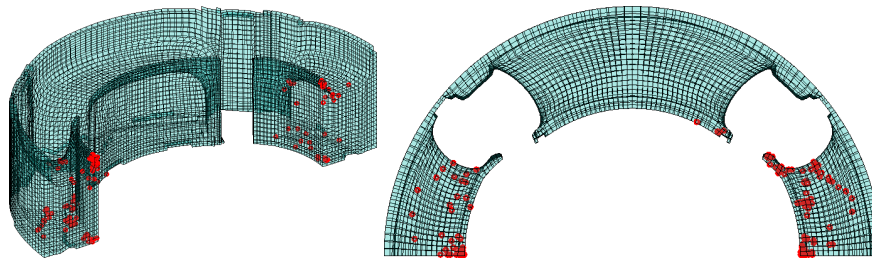


Figure 8: Localization of integration points selected by the hyper-reduction.

A second hyper-reduction was made for only half cycle, from 1/4 cycle to 3/4 cycle, of the full simulation to evaluate the possibility of using less data on learning phase. Figure 9 illustrates that outside the transition associated with the first quarter cycle, the match is still quite good. The differences in the first 1/4 cycle and the up part of the cycle are rather limited.

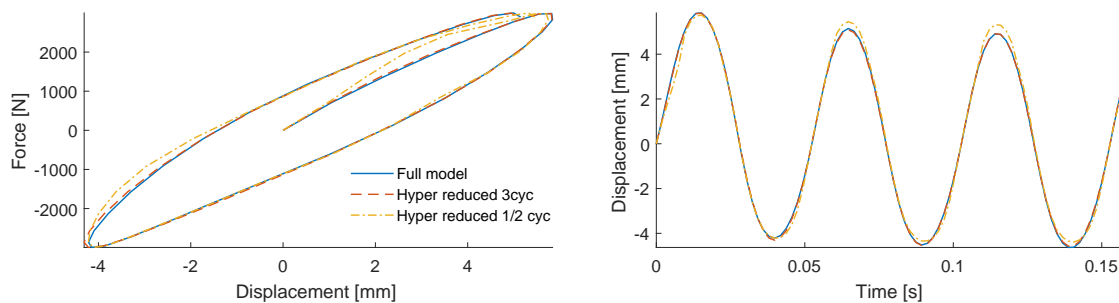


Figure 9: Comparison between the force displacement diagram and the displacement on time for full and hyper-reduced models.

The hyper reduced model is also accurate for predicting local deformations and stresses as illustrated by figure 10.

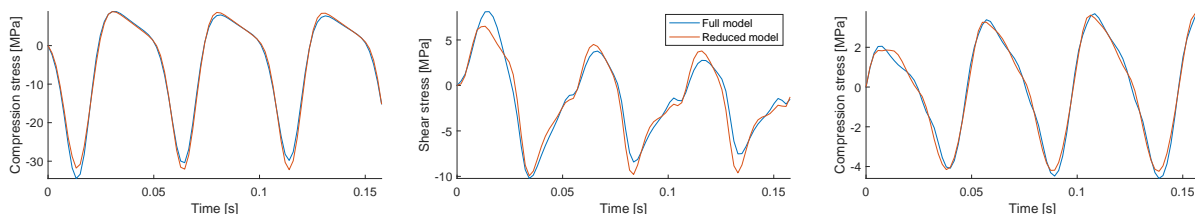


Figure 10: Stress comparison on three different points. The first on the center of the compressed zone, the second on the sheared zone and the last in the edge of the compressed zone.

Another benefit from hyper-reduction on explicit systems is the increased stability over timestep size, since smallest element length is no longer taken into consideration, and also, high frequency modes are filtered by the kinematic reduction. To illustrate the difference, articulation response for a force impulse in Ricker form with 5kN amplitude and 5ms duration is shown in figure 11. For the hyper-reduced model an explicit integration with a timestep increased by a factor 20 leads to a response with no visible difference.

4.3 Extrapolation accuracy

Harmonic loading at low frequency is an interesting tool for performance assessment in terms of comfort analysis, but there are other fields that require different solicitations. For example, lower amplitude and higher frequency solicitations may be pertinent for evaluating vehicle dynamic behavior when going over a

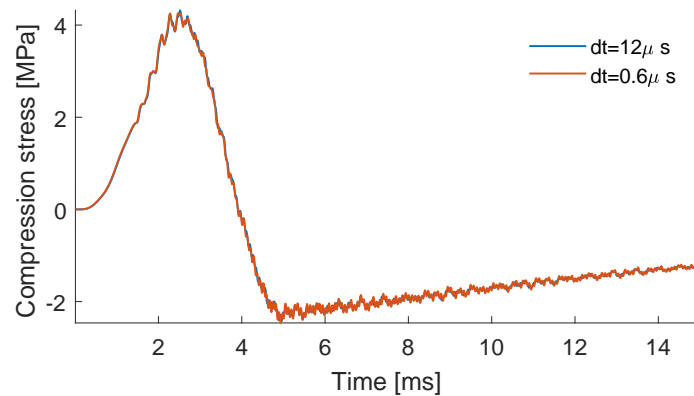


Figure 11: Articulation impulse response.

bumpy road. Figure 12 show the response to the articulation at 100Hz and 50N of amplitude. Both local and global behaviors are well represented by the hyper-reduced model, even if these conditions are very far from the learning conditions.

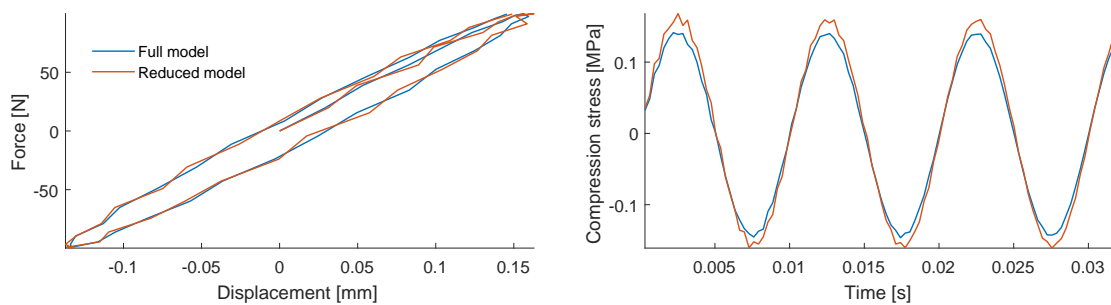


Figure 12: Articulation response to high frequency and low amplitude: global behavior on the left and localized stress on the right.

5 Conclusion

This first study clearly demonstrated the great potential of hyper-reduced models of rubber articulations. The 3 order of magnitude CPU speedup and memory decrease that was achieved, makes direct use for multi-body simulations a clear perspective. Efficient use will however require the development of proper strategies to build the learning subspace that are more evolved than the simple monoaxial harmonic response considered here. For different amplitudes and material constants, the results seem to be robust so far. But in the long term, one will need to account for multi-axial transient loading for a range of materials. Furthermore, geometry studies will be necessary to achieve the method full potential.

References

- [1] R. Penas, A. Gaudin, A. Kreis, and E. Balmes, “Dissipation in hysteretic rubber mount models,” Jun. 2019. [Online]. Available: <https://www.taylorfrancis.com/>
- [2] E. Balmes, *Structural Dynamics Toolbox (for Use with MATLAB)*. SDTools, Paris, Sep. 1995.
- [3] J. Diani, M. Brieu, and P. Gilormini, “Observation and modeling of the anisotropic visco-hyperelastic behavior of a rubberlike material,” *International Journal of Solids and Structures*, vol. 43,

- no. 10, pp. 3044–3056, May 2006. [Online]. Available: <http://linkinghub.elsevier.com/retrieve/pii/S0020768305003811>
- [4] F. Vincent, “Du modèle matériau à la mécanique des systèmes : étude dynamique d’une liaison souple en silicone chargée de silice,” Ph.D. dissertation, École Nationale Supérieure des Mines de Paris, 2011. [Online]. Available: <https://pastel.archives-ouvertes.fr/pastel-00584332>
 - [5] D. Wollscheid and A. Lion, “Predeformation- and frequency-dependent material behaviour of filler-reinforced rubber: Experiments, constitutive modelling and parameter identification,” *International Journal of Solids and Structures*, vol. 50, pp. 1217–1225, 2013.
 - [6] A. Ricker, N. H. Kroger, M. Ludwig, R. Landgraf, and J. Ihlemann, “Validation of a hyperelastic modelling approach for cellular rubber,” Jun. 2019. [Online]. Available: <https://www.taylorfrancis.com/>
 - [7] R. Bouaziz, C. Ovalle, and L. Laiarinandrasana, “A constitutive model for rubber bearings subjected to combined compression and shear,” Jun. 2019. [Online]. Available: <https://www.taylorfrancis.com/>
 - [8] S. Niroomandi, I. Alfaro, E. Cueto, and F. Chinesta, “Model order reduction for hyperelastic materials,” *INTERNATIONAL JOURNAL FOR NUMERICAL METHODS IN ENGINEERING*, May 2009. [Online]. Available: <http://amb.unizar.es/PDFs/Kirchhoff-SaintVenant.pdf>
 - [9] H. Dal, Y. Badienia, K. Açikgoz, F. A. Denli, Y. Badienia, K. Açikgoz, and F. A. Denli, “A comparative study on hyperelastic constitutive models on rubber: State of the art after 2006,” Jun. 2019. [Online]. Available: <https://www.taylorfrancis.com/>
 - [10] J. Schroder and P. Neff, “Invariant formulation of hyperelastic transverse isotropy based on polyconvex free energy functions,” *International Journal of Solids and Structures*, vol. 40, no. 2, pp. 401–445, Jan. 2003. [Online]. Available: <http://www.sciencedirect.com/science/article/pii/S0020768302004584>
 - [11] F. Renaud, J.-L. Dion, G. Chevallier, I. Tawfiq, and R. Lemaire, “A new identification method of viscoelastic behavior: Application to the generalized Maxwell model,” *Mechanical Systems and Signal Processing*, vol. 25, no. 3, pp. 991–1010, Apr. 2011. [Online]. Available: <http://www.sciencedirect.com/science/article/pii/S0888327010003079>
 - [12] J. C. Simo and T. J. R. Hughes, *Computational inelasticity*, 2nd ed., ser. Interdisciplinary applied mathematics Mechanics and materials. New York, NY: Springer, 2000, no. 7.
 - [13] D. Doyen, A. Ern, and S. Piperno, “A Semi-Explicit Modified Mass Method for Dynamic Frictionless Contact Problems,” in *Trends in Computational Contact Mechanics*, ser. Lecture Notes in Applied and Computational Mechanics, G. Zavarise and P. Wriggers, Eds. Berlin, Heidelberg: Springer, 2011, pp. 157–168. [Online]. Available: https://doi.org/10.1007/978-3-642-22167-5_9
 - [14] G. Vermot des Roches, “Frequency and time simulation of squeal instabilities. Application to the design of industrial automotive brakes.” Ph.D. dissertation, Ecole Centrale Paris, 2011.
 - [15] R. J. Craig, “A Review of Time-Domain and Frequency Domain Component Mode Synthesis Methods,” *Int. J. Anal. and Exp. Modal Analysis*, vol. 2, no. 2, pp. 59–72, 1987.
 - [16] E. Balmes, “Optimal Ritz vectors for component mode synthesis using the singular value decomposition,” *AIAA Journal*, vol. 34, no. 6, pp. 1256–1260, 1996.
 - [17] G. Kerschen, J.-c. Golinval, A. F. Vakakis, and L. A. Bergman, “The method of proper orthogonal decomposition for dynamical characterization and order reduction of mechanical systems: An overview,” *Nonlinear dynamics*, vol. 41, no. 1, pp. 147–169, 2005.
 - [18] F. Chinesta, A. Huerta, G. Rozza, and K. Willcox, “Model Reduction Methods,” in *Encyclopedia of Computational Mechanics Second Edition*, E. Stein, R. de Borst, and T. J. R. Hughes, Eds. Chichester, UK: John Wiley & Sons, Ltd, Dec. 2017, pp. 1–36.

- [19] S. T. Roweis, “Nonlinear Dimensionality Reduction by Locally Linear Embedding,” *Science*, vol. 290, no. 5500, pp. 2323–2326, Dec. 2000.
- [20] M. S. Allen, D. Rixen, M. van der Seijs, P. Tiso, T. Abrahamsson, and R. L. Mayes, “Model Reduction Concepts and Substructuring Approaches for Nonlinear Systems,” in *Substructuring in Engineering Dynamics: Emerging Numerical and Experimental Techniques*, ser. CISM International Centre for Mechanical Sciences, M. S. Allen, D. Rixen, M. van der Seijs, P. Tiso, T. Abrahamsson, and R. L. Mayes, Eds. Cham: Springer International Publishing, 2020, pp. 233–267. [Online]. Available: https://doi.org/10.1007/978-3-030-25532-9_6
- [21] C. Farhat, P. Avery, T. Chapman, and J. Cortial, “Dimensional reduction of nonlinear finite element dynamic models with finite rotations and energy-based mesh sampling and weighting for computational efficiency: NONLINEAR MODEL REDUCTION AND ENERGY-CONSERVING SAMPLING AND WEIGHTING,” *International Journal for Numerical Methods in Engineering*, vol. 98, no. 9, pp. 625–662, Jun. 2014. [Online]. Available: <http://doi.wiley.com/10.1002/nme.4668>
- [22] ABAQUS, *Standard User’s Manual, Version 6.9*. Dassault Systèmes Simulia Corp, 2016.

